Thermohydrodynamics of boiling in binary compressible fluids

Jiewei Liu,* Minh Do-Quang, and Gustav Amberg
Department of Mechanics, The Royal Institute of Technology, 100 44 Stockholm, Sweden
(Received 30 June 2015; published 23 October 2015)

We numerically study the thermohydrodynamics of boiling for a CO_2 + ethanol mixture on lyophilic and lyophobic surfaces in both closed and open systems, based on a diffuse interface model for a two-component system. The corresponding wetting boundary conditions for an isothermal system are proposed and verified in this paper. New phenomena due to the addition of another component, mainly the preferential evaporation of the more volatile component, are observed. In the open system and the closed system, the physical process shows very different characteristics. In the open system, except for the movement of the contact line, the qualitative features are rather similar for lyophobic and lyophilic surfaces. In the closed system, the vortices that are observed on a lyophobic surface are not seen on a lyophilic surface. More sophisticated wetting boundary conditions for nonisothermal, two-component systems might need to be further developed, taking into account the variations of density, temperature, and surface tension near the wall, while numerical results show that the boundary conditions proposed here also work well even in boiling, where the temperature is nonuniform.

DOI: 10.1103/PhysRevE.92.043017 PACS number(s): 47.55.db

I. INTRODUCTION

Boiling is of great importance due to its efficiency in heat transfer and has numerous applications in chemical or process industries, thermal power plants, and refrigeration systems [1,2]. Physically speaking, boiling is a complex process in which various physical phenomena are involved, like phase transitions, heat and mass transfer, nucleation, growth and departure of bubbles, and motion of the contact line on the solid surface [3]. Due to its importance in a variety of applications, as well as many complex and interesting associated physical phenomena, boiling has generated extensive research, both experimentally and numerically. Boiling involves very small spatial and temporal scales; making a precise experimental study rather limited [4]. Numerical simulation is thus of great significance as another effective way to study the thermohydrodynamics aspects of the boiling in detail.

Different methods have been applied to simulate the boiling process, like molecular dynamics [5] on a molecular scale, the lattice Boltzmann method [6,7] on a mesoscopic scale, and the continuum method [3,4,8–12] on a macroscopic scale. A big class of continuum methods is the front-capturing method, which captures the interface on a fixed grid [13]. The volume-of-fluid (VOF) method [14,15], the level set method [16,17], and the diffuse interface method [18] belong to this class. Examples of the simulation of boiling for incompressible flows include the work done by Kunkelmann and Stephan [10,11] using the VOF method, the work done by Son and Dhir [8] and Mukherjee and Kandlikar [9] using the level-set method, and the work done by Tomar *et al.* [4] using a coupled level-set and VOF method. In both the level-set method and the VOF method, the movement of the interface is described by an advection equation of an artificial variable, which is the distance function in the level-set method and the volume fraction function in the VOF method. The hyperbolic character of the advection equation sets a high demand on the numerical scheme.

The diffuse interface method is a different front-capturing method. It is generally more computationally expensive, but it has the advantages that other interface-capturing scheme do not have. It does not suffer from problems with an accurate calculation of surface tension [19]. Moreover, it is derived from a free-energy-based variational formalism, thus the resulting system of equations is well posed and satisfy thermodynamics-consistent energy dissipation laws [20]. Neither the level-set method nor the VOF method could maintain energy conservation [21]. It could be used to explore essential interfacial physics at the interfacial region [22]. Furthermore, the order parameter which could describe the position and thickness of the interface satisfies an advection-diffusion equation and thus is numerically easier to implement.

The idea of a diffuse or a nonzero-thickness interface could be traced back to van der Waals [23], whose work made the description of liquid-gas coexistence and transition possible. Since the work of Cahn and Hilliard [24], who introduced the gradient of composition into the free energy in order to study the interfacial structure of isothermal binary alloys, the diffuse interface method gained lots of attention and has now become one of the major tools to study a variety of interfacial phenomena [20]. Anderson *et al.* [18] gave a review of the contemporary diffuse interface method, and a general method to derive the hydrodynamic equations from the conservation laws and the second law of thermodynamics. Onuki [25] extended the van der Waals theory by considering that the liquid-gas transition could also happen in nonuniform temperature. Later, Onuki [26] extended his dynamic van der Waals theory to two-component systems by adding the gradient of density of each component to the free-energy functional, but without giving any hydrodynamic equations to describe the system with such a form of free energy.

Recently, Laurila *et al.* [12] and Xu and Qian [3] used diffuse interface method, which is the dynamic van der Waals model [25], to simulate the boiling process. Laurila *et al.* [12] studied the thermodynamics of boiling of water. Their main objective was to observe the difference between a closed and an open system, as well as the dynamics on hydrophobic and hydrophilic surfaces. Xu and Qian [3] also numerically investigated the boiling dynamics of a single vapor bubble in a pure fluid. They mainly studied the dynamics of a bubble on

*jiewei@mech.kth.se

a homogeneous surface with different contact angles or on a patterned surface, with or without an artificial gravity included.

All of the simulations we mentioned above are for a single-component fluid. It is found that some binary systems have better thermodynamic efficiency and heat transfer performance because they might show better resistance to dry out and the onset of film boiling [1,2]. Although boiling of a binary fluid is at least as significant as boiling of a single-component fluid, numerical study of a two-component boiling system is rather rare in literature, to the author's knowledge. With the addition of another component, more physical phenomena appear in the boiling process, like the interaction of different species, the preferential evaporation of the more volatile component, or the Marangoni flow that might be generated.

Following the idea in previous works [18,25,26], using the conservation laws and the principle of positive entropy production, as well as the thermodynamic relation for two components, Liu *et al.* [27] derived the hydrodynamic equations for two-component, compressible system. Based on this model, we are going to study the boiling of two-component fluids. Our main purpose here is to extend the boiling study for the pure fluid done by Lauria *et al.* [12] to two-component fluids and to observe some new phenomena that are caused by the addition of another component. With the use of the diffuse interface model, the multiple physical phenomena involved in the complex binary boiling process will appear automatically as an outcome of calculation.

The rest of this paper is organized as follows: We present the dimensional diffuse interface model for a two-component system in Sec. II A and the corresponding dimensionless model in Sec. II B. Wetting boundary conditions for an isothermal, two-component system are derived and verified in Secs. II C and II E, respectively. Section II D is about the numerical scheme. In Sec. III we shows our numerical simulation of the boiling in open and closed systems, with the surface being lyophilic or lyophobic. Section IV is the discussion. Section V is the conclusion.

II. PROBLEM FORMULATION

A. Governing equations in the bulk

The governing equations that we use is a model that has been proposed in our previous paper [27]. This model is derived based on the conservation laws (mass conservation, momentum conservation, energy conservation) and the second laws of thermodynamics (the positive entropy production), as well as the fundamental thermodynamic relation of a binary system. A detailed derivation can be found in the paper [27]. Here, we only give the resulting governing equations.

For a binary system, the Helmholtz free-energy functional can be defined as [26] (in the following, variables with or without $\sim$ are dimensional or dimensionless, respectively)

$$\tilde{\mathcal{F}}(\tilde{\rho}_1,\tilde{\rho}_2) = \int_{\tilde{V}} \left[\tilde{f}(\tilde{\rho}_1,\tilde{\rho}_2) + \frac{1}{2} \sum_{i,j\in\{1,2\}} \frac{k_B \tilde{T} \tilde{D}_{i,j}}{\tilde{m}_i \tilde{m}_j} \tilde{\nabla}\tilde{\rho}_i \cdot \tilde{\nabla}\tilde{\rho}_j \right] d\tilde{V}, \quad (1)$$

where $\tilde{V}$ is a control volume, $\tilde{f}(\tilde{\rho}_1,\tilde{\rho}_2)$ is the bulk free-energy density with $\tilde{\rho}_i$ being the density of the component i. $\tilde{m}_i$ represents the molecular mass of component i, coefficients $\tilde{D}_{i,j}$ in front of the gradient terms are related to the interfacial thickness and surface tension. The Helmholtz free-energy density $\tilde{f}(\tilde{\rho}_1,\tilde{\rho}_2)$ is given by [26]

$$\tilde{f}(\tilde{\rho}_1,\tilde{\rho}_2) = \tilde{T} \sum_i \frac{\tilde{\rho}_i}{\tilde{m}_i} \left[\ln\left(\frac{\tilde{\rho}_i \tilde{\lambda}_i^3}{\tilde{m}_i(1-\tilde{\phi})} \right) - 1 \right] - \sum_{i,j} \tilde{a}_{i,j} \frac{\tilde{\rho}_i}{\tilde{m}_i} \frac{\tilde{\rho}_j}{\tilde{m}_j}, \quad (2)$$

where $\tilde{\lambda}_i = (\frac{1}{2\pi \tilde{m}_i k_B \tilde{T}})^{1/2} \bar{h}$ are the de Broglie length and $\bar{h}$ is the Planck constant. $\tilde{\phi} = \sum_i \tilde{b}_i \frac{\tilde{\rho}_i}{\tilde{m}_i}$ is the volume fraction occupied by the molecules with $\tilde{b}_i$ being the molecular volume of component i [26]. The coefficients $\tilde{a}_{ij}$ measures the attraction forces between molecules of component i and component j.

The governing equations are the following:

Mass balance equation:

$$\frac{\tilde{\partial}\tilde{\rho}}{\tilde{\partial}\tilde{t}} + \tilde{\nabla}\cdot(\tilde{\rho}\tilde{\vec{\mathbf{v}}}) = 0, \quad (3)$$

$$\frac{\tilde{\partial}\tilde{\rho}_1}{\tilde{\partial}\tilde{t}} + \tilde{\nabla}\cdot(\tilde{\rho}_1\tilde{\vec{\mathbf{v}}}) = \tilde{\nabla}\cdot\left[\tilde{M}_J \tilde{\nabla}\left(\frac{\tilde{\hat{\mu}}_1 - \tilde{\hat{\mu}}_2}{\tilde{T}} \right) \right]. \quad (4)$$

Momentum equation:

$$\frac{\tilde{\partial}(\tilde{\rho}\tilde{\vec{\mathbf{v}}})}{\tilde{\partial}\tilde{t}} + \tilde{\nabla}\cdot(\tilde{\rho}\tilde{\vec{\mathbf{v}}}\tilde{\vec{\mathbf{v}}}) = \tilde{\nabla}\cdot(\tilde{\overleftrightarrow{P}} + \tilde{\overleftrightarrow{\tau}}). \quad (5)$$

Full energy equation:

$$\frac{\tilde{\partial}(\tilde{\rho}\tilde{e_T})}{\tilde{\partial}\tilde{t}} + \tilde{\nabla}\cdot(\tilde{\rho}\tilde{e_T}\tilde{\vec{\mathbf{v}}}) = \tilde{\nabla}\cdot[(\tilde{\overleftrightarrow{P}} + \tilde{\overleftrightarrow{\tau}})\cdot\tilde{\vec{\mathbf{v}}}] + \tilde{\nabla}\cdot(\tilde{\kappa}\tilde{\nabla}\tilde{T}) - \sum_{i,j\in\{1,2\}} \tilde{\nabla}\cdot\left(\frac{k_B\tilde{T}\tilde{D}_{i,j}}{\tilde{m}_i\tilde{m}_j} \frac{d\tilde{\rho}_i}{d\tilde{t}} \tilde{\nabla}\tilde{\rho}_j \right). \quad (6)$$

In the equations above, the generalized pressure tensor $\tilde{\overleftrightarrow{P}}$ in equations (5) and (6) is

$$\tilde{\overleftrightarrow{P}} = -\tilde{p}\,\tilde{\overleftrightarrow{\mathcal{I}}} + \tilde{\overleftrightarrow{P}}_D, \quad (7)$$

$$\tilde{\overleftrightarrow{P}}_D = \tilde{\mathcal{L}}_D \tilde{\overleftrightarrow{\mathcal{I}}} - \frac{\tilde{\partial}\tilde{\mathcal{L}}_D}{\tilde{\partial}\tilde{\nabla}\tilde{\rho}_1} \otimes \tilde{\nabla}\tilde{\rho}_1 - \frac{\tilde{\partial}\tilde{\mathcal{L}}_D}{\tilde{\partial}\tilde{\nabla}\tilde{\rho}_2} \otimes \tilde{\nabla}\tilde{\rho}_2, \quad (8)$$

where

$$\tilde{\mathcal{L}}_D(\tilde{\rho}_1,\tilde{\rho}_2) = \sum_{i,j\in\{1,2\}} \tilde{\rho}_i \tilde{\nabla}\cdot\left(\frac{k_B\tilde{T}\tilde{D}_{i,j}}{\tilde{m}_i\tilde{m}_j} \tilde{\nabla}\tilde{\rho}_j \right) + \frac{1}{2} \sum_{i,j\in\{1,2\}} \frac{k_B\tilde{T}\tilde{D}_{i,j}}{\tilde{m}_i\tilde{m}_j} \tilde{\nabla}\tilde{\rho}_i \cdot \tilde{\nabla}\tilde{\rho}_j. \quad (9)$$

The thermodynamic pressure $\tilde{p}$ in Eq. (7) is

$$\tilde{p} = \tilde{\rho}_1 \frac{\tilde{\partial}\tilde{f}(\tilde{\rho}_1,\tilde{\rho}_2)}{\tilde{\partial}\tilde{\rho}_1} + \tilde{\rho}_2 \frac{\tilde{\partial}\tilde{f}(\tilde{\rho}_1,\tilde{\rho}_2)}{\tilde{\partial}\tilde{\rho}_2} - \tilde{f}(\tilde{\rho}_1,\tilde{\rho}_2). \quad (10)$$

The generalized chemical potential $\tilde{\hat{\mu}}_i$ in Eq. (4) is

$$\tilde{\hat{\mu}}_i = \tilde{\mu}_i - \sum_j \frac{k_B \tilde{T} \tilde{D}_{i,j}}{\tilde{m}_i \tilde{m}_j} \tilde{\nabla}^2 \tilde{\rho}_j, \tag{11}$$

with

$$\tilde{\mu}_i = \frac{\partial \tilde{f}(\tilde{\rho}_1, \tilde{\rho}_2)}{\partial \tilde{\rho}_i} \tag{12}$$

being the chemical potential of species i in the bulk.

$\tilde{M}_J$ in Eq. (4) is defined as

$$\tilde{M}_J = \tilde{M}_f \frac{\tilde{\rho}_1 \tilde{\rho}_2}{\tilde{\rho}^2}, \tag{13}$$

where $\tilde{M}_f$ is the mobility coefficient [28].

The viscous stress tensor in Eqs. (5) and (6) is

$$\overleftrightarrow{\tilde{\tau}} = \tilde{\eta}(\tilde{\nabla}\tilde{\vec{\mathbf{v}}} + \tilde{\nabla}\tilde{\vec{\mathbf{v}}}^{\perp}) + (\tilde{\xi} - 2\tilde{\eta}/3)\overleftrightarrow{\tilde{\mathcal{I}}}\,\tilde{\nabla} \cdot \tilde{\vec{\mathbf{v}}}, \tag{14}$$

where $\tilde{\eta}$ and $\tilde{\xi}$ are the shear and bulk viscosity, respectively, and are assumed to be the same in this paper. For a one-component system, Onuki [25] and Laurila *et al.* [12] assumed that both $\tilde{\eta}$ and the heat conductivity $\tilde{\kappa}$ linearly depend on the density, i.e., $\tilde{\eta} = \tilde{\eta}_0 \rho$, $\tilde{\kappa} = \tilde{\kappa}_0 \rho$, where $\tilde{\eta}_0$ is the kinematic viscosity, $\tilde{\kappa}_0$ is the heat conductivity per unit density. For two-component systems, for simplicity, we assume that $\tilde{\eta} = \tilde{\eta}_{0,1}\rho_1 + \tilde{\eta}_{0,2}\rho_2$, $\tilde{\kappa} = \tilde{\kappa}_{0,1}\rho_1 + \tilde{\kappa}_{0,2}\rho_2$, where $\tilde{\eta}_{0,i}$, $\tilde{\kappa}_{0,i}$ are the kinematic viscosity and the heat conductivity per unit density for component i.

The specific total energy $\tilde{e_T}$ in Eq. (6) satisfies

$$\tilde{\rho}\tilde{e_T} = \tilde{\rho}\tilde{e} + \tfrac{1}{2}\tilde{\rho}\tilde{\vec{\mathbf{v}}}^2. \tag{15}$$

And the specific internal energy $\tilde{e}$ in Eq. (15) satisfies

$$\tilde{\rho}\tilde{e} = \tilde{f} - \tilde{T}\frac{\partial \tilde{f}}{\partial \tilde{T}}. \tag{16}$$

B. Dimensionless formulation

The equations (3)–(6) and related formulas (7)–(16) are made dimensionless based on the following scaling

$$\begin{aligned} &\tilde{\rho} = \rho^* \rho, \quad \tilde{\vec{\mathbf{v}}} = v^* \vec{\mathbf{v}}, \quad \tilde{x} = L^* x, \quad \tilde{y} = L^* y, \\ &\tilde{p} = p^* p, \quad \tilde{T} = T^* T, \quad \tilde{e} = \frac{p^*}{\rho^*} e. \end{aligned} \tag{17}$$

The characteristic variables that we choose are basically similar to those chosen by Laurila *et al.* [12]. Now we have two components in the system, we choose the property of the second component for the scaling. ρ^*, p^*, T^* is the critical point of the second component, so $\rho^* = \frac{\tilde{m}_2}{3\tilde{b}_2}$, $p^* = \frac{\tilde{a}_{22}}{27\tilde{b}_2^2}$, and $T^* = \frac{8\tilde{a}_{22}}{27 k_B \tilde{b}_2}$. The characteristic length $L^* = 2\tilde{b}_2^{1/3}$, which is on the order of interfacial thickness. Characteristic velocity v^* is chosen to be the sound speed at the critical point of the second component. By introducing the scaling (17) into equations (3)–(6) and other formulas (7)–(16), we obtain their corresponding dimensionless form:

The mass balance equation,

$$0 = \frac{\partial \rho}{\partial t} + \nabla \cdot (\rho \vec{\mathbf{v}}), \tag{18}$$

$$\frac{\partial \rho_1}{\partial t} + \nabla \cdot (\rho_1 \vec{\mathbf{v}}) = \nabla \cdot \left[M_f \frac{\rho_1 \rho_2}{\rho^2} \nabla \left(\frac{\hat{\mu}_1 - \hat{\mu}_2}{T} \right) \right], \tag{19}$$

the momentum balance equation,

$$\frac{\partial (\rho \vec{\mathbf{v}})}{\partial t} + \nabla \cdot (\rho \vec{\mathbf{v}} \vec{\mathbf{v}}) = \mathcal{R} \nabla \cdot \overleftrightarrow{P} + \frac{1}{\mathcal{R}e} \nabla \cdot \overleftrightarrow{\tau}, \tag{20}$$

and the full energy equation,

$$\begin{aligned} &\frac{\partial (\rho e_T)}{\partial t} + \nabla \cdot (\rho e_T \vec{\mathbf{v}}) \\ &\quad = \nabla \cdot \left[\left(\overleftrightarrow{P} + \frac{1}{\mathcal{R}e \cdot \mathcal{R}} \overleftrightarrow{\tau} \right) \cdot \vec{\mathbf{v}} \right] \\ &\qquad + \mathcal{B} \nabla \cdot [(\kappa_{12}\rho_1 + \rho_2) \nabla T] \\ &\qquad - \sum_{i,j \in \{1,2\}} \nabla \cdot \left(\frac{T D_{i,j}}{m_i m_j} \frac{d\rho_i}{dt} \nabla \rho_j \right), \end{aligned} \tag{21}$$

In the equations above, the generalized pressure tensor $\overleftrightarrow{P}$ in equations (20) and (21) is

$$\overleftrightarrow{P} = -p \overleftrightarrow{\mathcal{I}} + \overleftrightarrow{P}_D, \tag{22}$$

$$\overleftrightarrow{P}_D = \mathcal{L}_D \overleftrightarrow{\mathcal{I}} - \frac{\partial \mathcal{L}_D}{\partial \nabla \rho_1} \otimes \nabla \rho_1 - \frac{\partial \mathcal{L}_D}{\partial \nabla \rho_2} \otimes \nabla \rho_2, \tag{23}$$

where

$$\begin{aligned} \mathcal{L}_D = &\sum_{i,j \in \{1,2\}} \rho_i \nabla \cdot \left(\frac{T D_{i,j}}{m_i m_j} \nabla \rho_j \right) \\ &+ \frac{1}{2} \sum_{i,j \in \{1,2\}} \frac{T D_{i,j}}{m_i m_j} \nabla \rho_i \cdot \nabla \rho_j. \end{aligned} \tag{24}$$

The thermodynamic pressure p in Eq. (22) is

$$p = \rho_1 \frac{\partial f(\rho_1, \rho_2)}{\partial \rho_1} + \rho_2 \frac{\partial f(\rho_1, \rho_2)}{\partial \rho_2} - f(\rho_1, \rho_2). \tag{25}$$

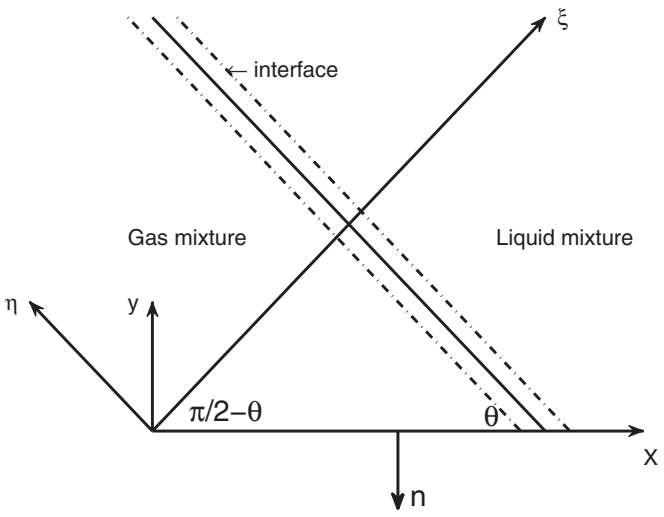

FIG. 1. Sketch of the geometry of an interface.

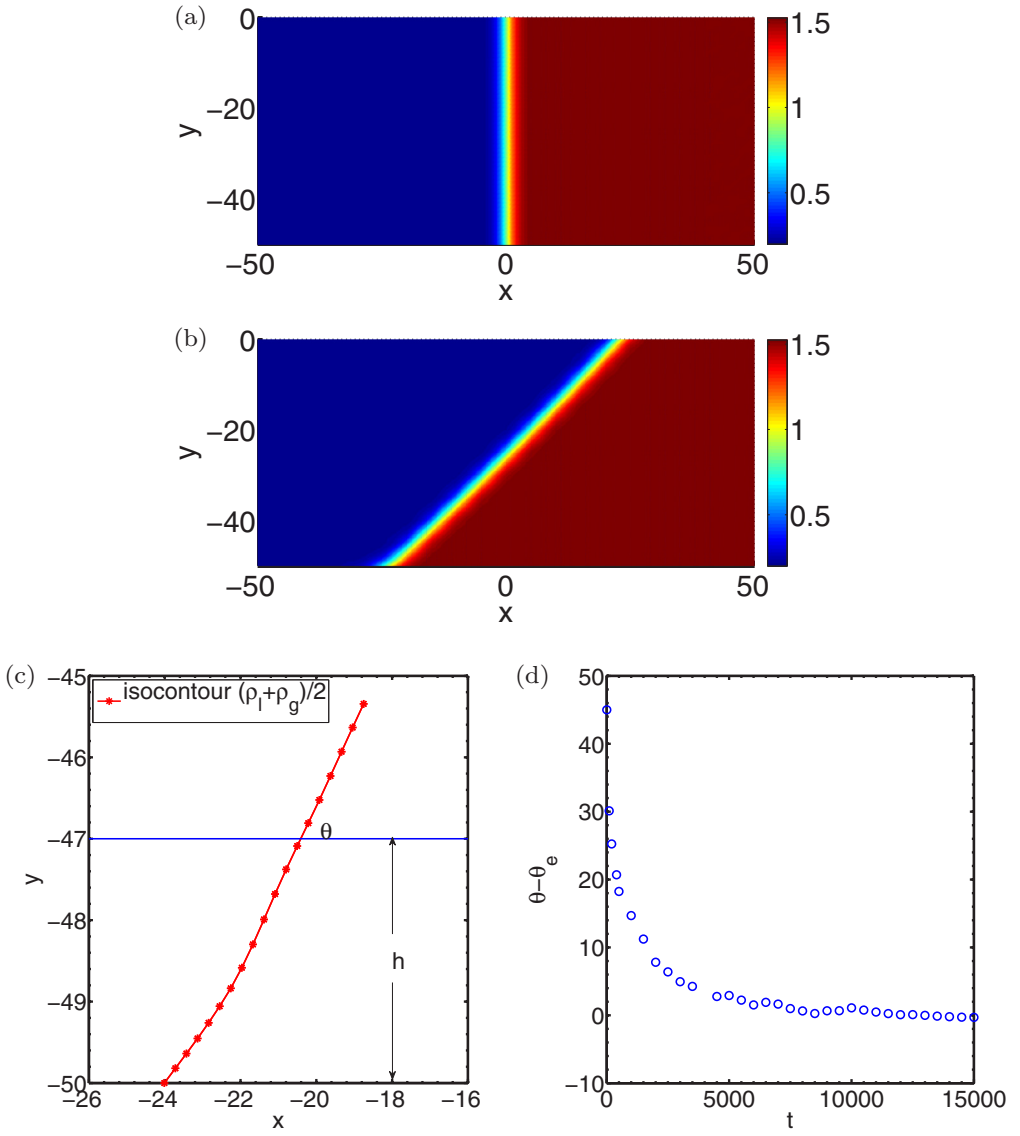

FIG. 2. (Color online) CO_2 + ethanol in an isothermal system, $T = 0.957$, $P = 0.4$. At the lower and upper wall, the equilibrium contact angles are $\theta_e = 45^\circ$ and $\theta_e = 135^\circ$, respectively. (a) Total density ρ at $t = 0$; (b) total density ρ at $t = 15\,000$. (c) The apparent contact angle θ measured at a distance h above the bottom wall, h is the interfacial thickness. (d) The difference between the apparent contact angle and the equilibrium contact angle $\theta - \theta_e$ vs time t.

The generalized chemical potential $\hat{\mu}_i$ in equation (19) is

$$\hat{\mu}_i = \mu_i - \sum_j \frac{T D_{i,j}}{m_i m_j} \nabla^2 \rho_j. \tag{26}$$

The viscous stress tensor in equations (20) and (21) is

$$\overleftrightarrow{\tau} = (\eta_{12}\rho_1 + \rho_2)(\nabla\vec{\mathbf{v}} + \nabla\vec{\mathbf{v}}^{\perp}) + \tfrac{1}{3}(\eta_{12}\rho_1 + \rho_2)\overleftrightarrow{\mathcal{I}}\nabla\cdot\vec{\mathbf{v}}. \tag{27}$$

The specific total energy e_T in equation (21) satisfies

$$\rho e_T = \rho e + \frac{1}{2\mathcal{R}}\rho\vec{\mathbf{v}}^2, \tag{28}$$

and the specific internal energy e in equation (28) satisfies

$$\rho e = f - T\frac{\partial f}{\partial T}. \tag{29}$$

Dimensionless parameters introduced in Eqs. (18)–(29) are the Reynolds number $\mathcal{R}e = \frac{L^* v^*}{\tilde{\eta}_2}$, which is the ratio between the inertial force and viscous force, the parameter $\mathcal{R} = \frac{p^*}{\rho^* v^{*2}}$, which is proportional to the ratio of the attractive potential energy to the molecular kinetic energy, the parameter $\mathcal{B} = \frac{\tilde{\kappa}_2 \rho^* T^*}{e^* v^* L^*}$, the ratio of the kinematic viscosity between two components $\eta_{12} = \frac{\eta_{0,1}}{\eta_{0,2}}$, the ratio of the thermal conductivity $\kappa_{12} = \frac{\kappa_{0,1}}{\kappa_{0,2}}$, the parameter $D_{i,j} = \frac{\tilde{D}_{i,j} k_B T^* \rho^{*2}}{m^{*2} L^{*2} p^*}$, which is related to the surface tension and interfacial thickness, and the mobility coefficient $M_f = \frac{p^* \tilde{M}_f}{L^* v^* \rho^{*2} T^*}$.

C. Wetting boundary condition

For the Cahn–Hilliard model, a wetting boundary condition can be derived from the total free energy of the system [29].

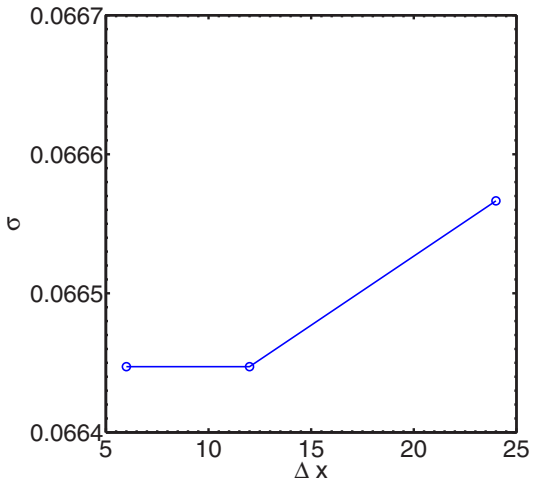

FIG. 3. (Color online) Dimensionless surface tension σ vs initial uniform mesh size Δx, where $\Delta x = 24$, 12, and 6, respectively. The minimum mesh size in the adaptive region is $h_m = 1$.

A similar methodology was applied to a one-component van der Waals fluid by Laurila *et al.* [12]. In this section, starting from the total free energy of the system, we are going to derive the wetting boundary condition for the two-component system.

Assume that γ_{sg} and γ_{sl} represent the surface energy per unit area between the solid and the gas and the solid and the liquid, respectively. By including the surface energy at the wall, the total free energy of the two-component system is

$$\hat{\mathcal{F}}(\rho_1,\rho_2)=\int_V \hat{f}(\rho_1,\rho_2)dV+\int_S[\gamma_{sg}+(\gamma_{sl}-\gamma_{sg})g(\rho)]dA, \tag{30}$$

where

$$\hat{f}(\rho_1,\rho_2)=f(\rho_1,\rho_2)+\frac{1}{2}\sum_{i,j\in\{1,2\}}\kappa_{ij}\nabla\rho_i\cdot\nabla\rho_j, \tag{31}$$

$\kappa_{ij}=\frac{k_BTD_{i,j}}{m_im_j}$ is constant for an isothermal system, and $g(\rho)$ is a function which satisfies $g(\rho^g)=0$ and $g(\rho^l)=1$, where $\rho=\rho_1+\rho_2$. So

$$\begin{aligned}\delta\hat{F}=&\int_V dV\left\{\left[\frac{\partial\hat{f}}{\partial\rho_1}-\nabla\cdot\left(\frac{\partial\hat{f}}{\partial(\nabla\rho_1)}\right)\right]\delta\rho_1\right\}\\&+\int_S dA\left(\frac{\partial\hat{f}}{\partial(\nabla\rho_1)}\cdot\boldsymbol{n}+(\gamma_{sl}-\gamma_{sg})\frac{\partial g}{\partial\rho_1}\right)\delta\rho_1\\&+\int_V dV\left\{\left[\frac{\partial\hat{f}}{\partial\rho_2}-\nabla\cdot\left(\frac{\partial\hat{f}}{\partial(\nabla\rho_2)}\right)\right]\delta\rho_2\right\}\\&+\int_S dA\left(\frac{\partial\hat{f}}{\partial(\nabla\rho_2)}\cdot\boldsymbol{n}+(\gamma_{sl}-\gamma_{sg})\frac{\partial g}{\partial\rho_2}\right)\delta\rho_2,\end{aligned} \tag{32}$$

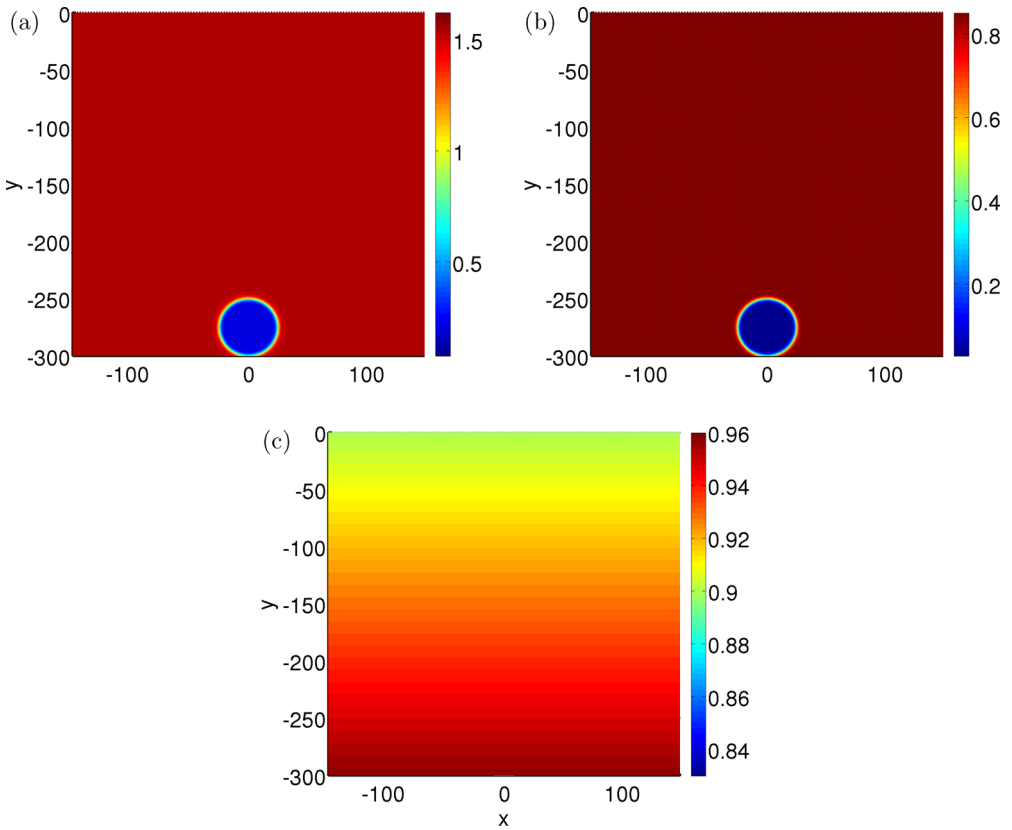

FIG. 4. (Color online) CO_2 + ethanol system at $T = 0.957$, $P = 0.4$, time $t = 0$. (a) Total density ρ, (b) density of ethanol ρ_1, (c) temperature T.

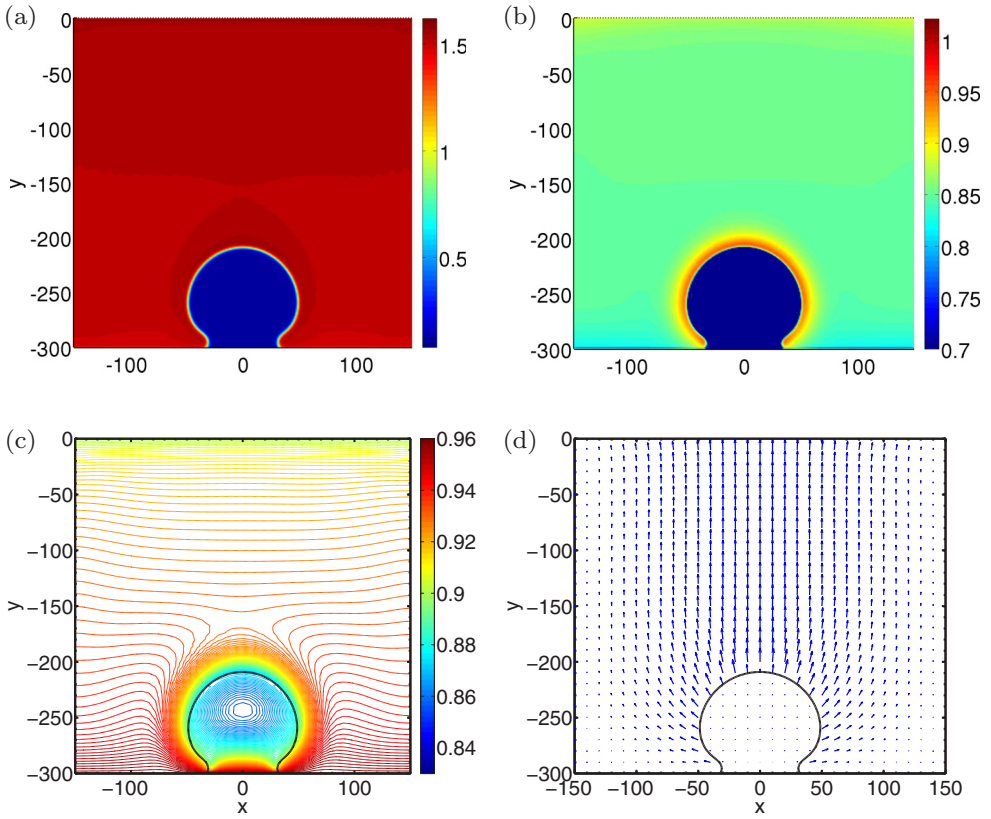

FIG. 5. (Color online) Case A: CO_2 + ethanol, open system, lyophobic surface; $t = 500$. (a) Total density ρ, (b) density of ethanol ρ_1 (a minimum value 0.7 is set in order to show the variation of ρ_1 around the interface), (c) contour of temperature T; black line represents the interface, (d) total mass flux $\rho\vec{\mathbf{v}}$.

and the wetting boundary conditions are

$$\frac{\partial \hat{f}}{\partial(\nabla\rho_1)}\cdot\boldsymbol{n} + (\gamma_{sl}-\gamma_{sg})\frac{\partial g}{\partial\rho_1} = 0, \tag{33}$$

$$\frac{\partial \hat{f}}{\partial(\nabla\rho_2)}\cdot\boldsymbol{n} + (\gamma_{sl}-\gamma_{sg})\frac{\partial g}{\partial\rho_2} = 0. \tag{34}$$

From the definition (31), Eqs. (33) and (34) become

$$(\kappa_{11}\nabla\rho_1 + \kappa_{12}\nabla\rho_2)\cdot\boldsymbol{n} + (\gamma_{sl}-\gamma_{sg})\frac{\partial g}{\partial\rho_1} = 0, \tag{35}$$

$$(\kappa_{21}\nabla\rho_1 + \kappa_{22}\nabla\rho_2)\cdot\boldsymbol{n} + (\gamma_{sl}-\gamma_{sg})\frac{\partial g}{\partial\rho_2} = 0. \tag{36}$$

We will show soon that, for our two-component system, the following relationship that is applicable to Cahn–Hilliard system still holds:

$$\gamma_{sg} - \gamma_{sl} = \sigma\cos\theta_e, \tag{37}$$

where σ is the surface tension between the liquid and gas mixture of the two components, θ_e is the equilibrium contact angle, defined as the angle between the liquid-gas interface and the solid wall on the liquid side. So finally, the wetting boundary conditions of the two component system (35) and (36) become

$$(\kappa_{11}\nabla\rho_1 + \kappa_{12}\nabla\rho_2)\cdot\boldsymbol{n} = \sigma\cos\theta_e\frac{\partial g}{\partial\rho_1}, \tag{38}$$

$$(\kappa_{21}\nabla\rho_1 + \kappa_{22}\nabla\rho_2)\cdot\boldsymbol{n} = \sigma\cos\theta_e\frac{\partial g}{\partial\rho_2}. \tag{39}$$

In the rest of the section, we are going to first prove the formula (37) and then shortly discuss the conditions for constructing the function $g(\rho)$.

Suppose the interface shape at the equilibrium is as shown in Fig. 1. The solid wall coincides with the x axis. The interface of the liquid and gas mixtures intersects with the solid wall at some point. $\boldsymbol{n}$ is the outward normal. The equilibrium contact angle satisfies $\theta_e = \pi - \theta$.

Rotate the current x-y coordinate system by an angle $\frac{\pi}{2} - \theta$, and assume that the new coordinates are ξ-η. From Fig. 1, we know that

$$\begin{aligned}\xi &= x\sin\theta + y\cos\theta,\\ \eta &= -x\cos\theta + y\sin\theta.\end{aligned} \tag{40}$$

Clearly, ξ is the direction normal to the interface, and η is the direction parallel to the interface. It is reasonable to assume that there is no variation in densities ρ, ρ_1, and ρ_2 in the η direction, so we can consider them to be a one-dimensional

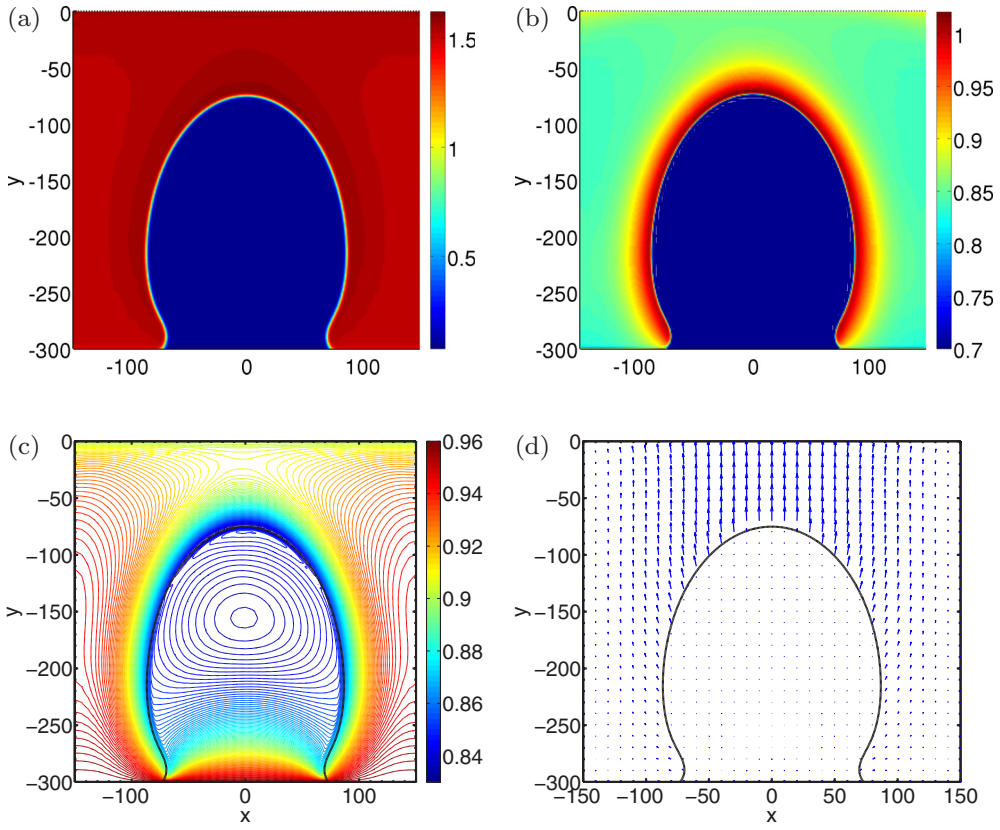

FIG. 6. (Color online) Case A: CO_2 + ethanol, open system, lyophobic surface; $t = 1500$. (a) Total density ρ, (b) density of ethanol ρ_1 (a minimum value 0.7 is set in order to show the variation of ρ_1 around the interface), (c) contour of temperature T; black line represents the interface, (d) total mass flux $\rho\vec{\mathbf{v}}$.

function in ξ. Then we have

$$(\kappa_{11}\nabla\rho_1 + \kappa_{12}\nabla\rho_2)\cdot\boldsymbol{n} = -\left(\kappa_{11}\frac{\partial\rho_1}{\partial\xi} + \kappa_{12}\frac{\partial\rho_2}{\partial\xi}\right)\frac{\partial\xi}{\partial y}, \quad (41)$$

$$(\kappa_{21}\nabla\rho_1 + \kappa_{22}\nabla\rho_2)\cdot\boldsymbol{n} = -\left(\kappa_{21}\frac{\partial\rho_1}{\partial\xi} + \kappa_{22}\frac{\partial\rho_2}{\partial\xi}\right)\frac{\partial\xi}{\partial y}. \quad (42)$$

So the wetting boundary conditions (35) and (36) become

$$-\left(\kappa_{11}\frac{\partial\rho_1}{\partial\xi} + \kappa_{12}\frac{\partial\rho_2}{\partial\xi}\right)\frac{\partial\xi}{\partial y} = (\gamma_{sg} - \gamma_{sl})\frac{\partial g}{\partial\rho_1}, \quad (43)$$

$$-\left(\kappa_{21}\frac{\partial\rho_1}{\partial\xi} + \kappa_{22}\frac{\partial\rho_2}{\partial\xi}\right)\frac{\partial\xi}{\partial y} = (\gamma_{sg} - \gamma_{sl})\frac{\partial g}{\partial\rho_2}. \quad (44)$$

Multiplying the formula (43) by $\frac{\partial\rho_1}{\partial\xi}$ and the formula (44) by $\frac{\partial\rho_2}{\partial\xi}$, adding them together, and noticing that $\frac{\partial\xi}{\partial y} = \cos\theta$, we obtain

$$-\left[\kappa_{11}\left(\frac{\partial\rho_1}{\partial\xi}\right)^2 + \kappa_{12}\frac{\partial\rho_1}{\partial\xi}\frac{\partial\rho_2}{\partial\xi} + \kappa_{22}\left(\frac{\partial\rho_2}{\partial\xi}\right)^2\right]\cos\theta = (\gamma_{sg} - \gamma_{sl})\frac{dg}{d\xi}. \quad (45)$$

Integrating formula (45) along the ξ direction from the gas mixture to the liquid mixture, applying the conditions $g(\xi_g) = 0$ and $g(\xi_l) = 1$, and noticing the fact that

$$\sigma = \int_{\xi_g}^{\xi_l}\kappa_{11}\left(\frac{\partial\rho_1}{\partial\xi}\right)^2 + \kappa_{12}\frac{\partial\rho_1}{\partial\xi}\frac{\partial\rho_2}{\partial\xi} + \kappa_{22}\left(\frac{\partial\rho_2}{\partial\xi}\right)^2 d\xi \quad (46)$$

is nothing else but the formula to calculate the surface tension for a binary system [30], we finally obtain

$$\gamma_{sg} - \gamma_{sl} = -\sigma\cos\theta = \sigma\cos(\pi - \theta) = \sigma\cos\theta_e. \quad (47)$$

By now, we finish the proof of the formula (37).

Now the remaining question is how to choose the function g in the conditions (38) and (39). Note that, in the Cahn–Hilliard model, the bulk free energy is $F(C) = \int\beta\Psi(C) + \frac{\alpha}{2}|\nabla C|^2 dV$, where $\Psi(C)$ is a fourth-order polynomial, and C represents the composition [29,31]. Thanks to the simple analytical solution of the equilibrium profile $C(\xi) = [\frac{2\beta}{\alpha}\Psi(C)]^{1/2}$ in the direction ξ, as well as the simple relationship that can be obtained between the surface tension σ and the parameters of the C-H model $\sigma = \frac{2\sqrt{2}}{3}\sqrt{\alpha\beta}$, $g(C)$ can be derived starting from the boundary condition $\alpha\nabla C\cdot\boldsymbol{n} = \sigma\cos\theta_e g'(C)$, giving a third-order polynomial of C. For more details, please refer to Carlson's work [31]. In a one- or two-component van der Waals fluid, due to the complicated form of the bulk free energy, no such a simple analytical solution of the equilibrium profile $\rho_i(\xi), i = 1,2$ can be obtained. Actually, it can be shown that, for the two-component system, at equilibrium, the inverse

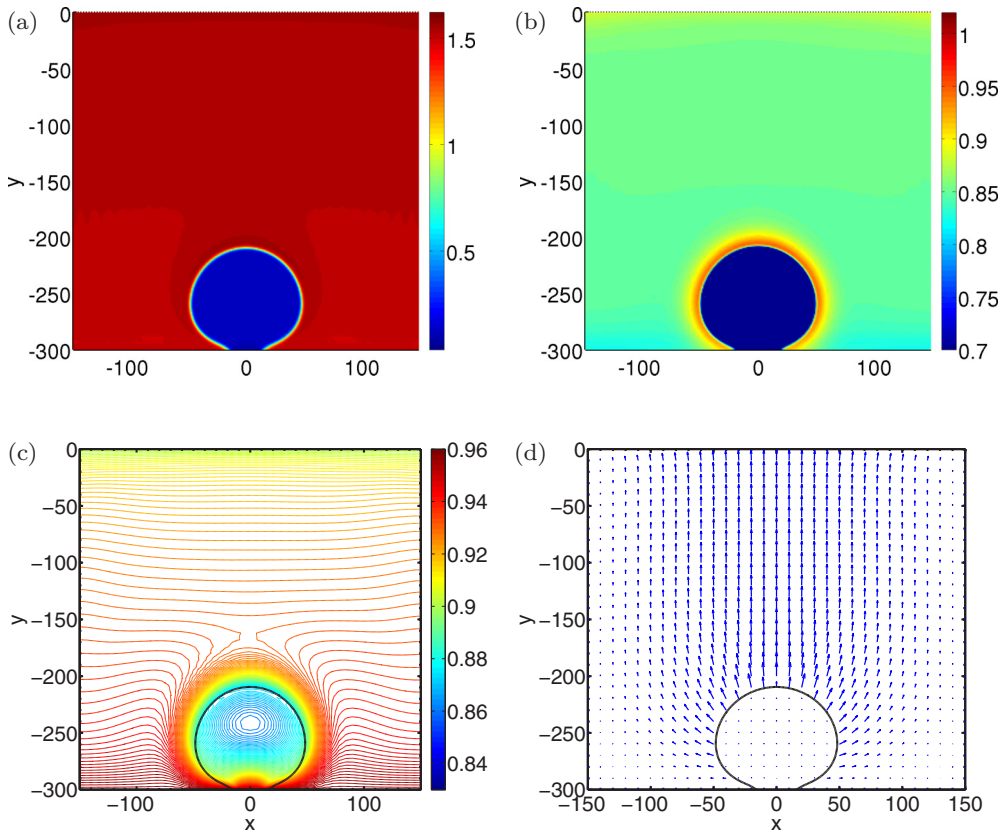

FIG. 7. (Color online) Case B: CO_2 + ethanol, open system, lyophilic surface; $t = 500$. (a) Total density ρ, (b) density of ethanol ρ_1 (a minimum value 0.7 is set in order to show the variation of ρ_1 around the interface), (c) contour of temperature T; black line represents the interface, (d) total mass flux $\rho\vec{\mathbf{v}}$.

functions of $\rho_1(\xi)$, $\rho_2(\xi)$ satisfy [30,32]

$$\xi(\rho_i) = \xi\left(\rho_i^g\right) + \int_{\rho_i^g}^{\rho_i} \sqrt{\frac{\sum_{j,k=1}^{2} \kappa_{kj} \frac{d\rho_k}{d\rho_i}\frac{d\rho_j}{d\rho_i}}{\Delta f}} d\rho_i, \qquad (48)$$

and $\frac{d\rho_2}{d\rho_1}$ satisfies the following differential equation:

$$\begin{aligned} 0 = &\left[\kappa_{11} + 2\kappa_{12}\frac{d\rho_2}{d\rho_1} + \kappa_{22}\left(\frac{d\rho_2}{d\rho_1}\right)^2\right] \\ &\times\left[\frac{\partial(\Delta f)}{\partial\rho_2}\left(\kappa_{11} + \kappa_{12}\frac{d\rho_2}{d\rho_1}\right) - \frac{\partial(\Delta f)}{\partial\rho_1}\left(\kappa_{12} + \kappa_{22}\frac{d\rho_2}{d\rho_1}\right)\right] \\ &- \frac{d^2\rho_2}{d\rho_1^2}[2(\kappa_{11}\kappa_{22} - \kappa_{12})\Delta f], \end{aligned} \qquad (49)$$

where

$$\Delta f = f(\rho_1, \rho_2) - \mu_1^e\rho_1 - \mu_2^e\rho_2 + P^{cx}, \qquad (50)$$

and μ_i^e is the chemical potential for component i at the coexistence pressure P^{cx}. No analytical solution for $\rho_1(\xi)$, $\rho_2(\xi)$ can be obtained from Eqs. (48)–(50). So no analytical formula of $g(\rho)$ can be obtained from the form of the bulk free energy f if following the same method of deriving the function $g(C)$ in the C-H case. But, just as what was done by Laurila *et al.* [12] for the one-component case, we can still use a third-order polynomial $g(\rho)$ as an approximation. In addition to the two conditions that have been proposed at the beginning of the Sec. II C, i.e., $g(\rho^g) = 0$ and $g(\rho^l) = 1$, the other two requirements on g are $\frac{\partial g}{\partial\rho}(\rho^l) = 0$ and $\frac{\partial g}{\partial\rho}(\rho^v) = 0$ far from the interface, which are obvious from formulas (43) and (44).

D. Numerical scheme

A finite element numerical toolbox FEMLEGO [33] together with the DEAL.II [34] have been used for all simulations. FEMLEGO is a symbolic tool for solving partial differential equations by using the finite element method. Equations, initial conditions and boundary conditions, and a linear solver are defined in a single Maple sheet. The source code that works with the DEAL.II library, will be generated automatically after compiling the Maple sheet. With two-component system, the generalized pressure tensor is more complicated than that of one-component system, and we have one more equation to describe the density variation of component 1. Other than these, other equations are similar to the one-component system. The numerical scheme is basically the same as used previously for a one-component van der Waals fluid [12,35,36], the characteristic-based split (CBS) method. Variables are discretized in space with piece-wise linear base functions. Time marching is the first-order Euler forward scheme. The numerical steps are the following, where the variables with a superscript n represent their values at time $n \triangle t$, $\vec{\mathbf{U}} = \rho\mathbf{v}$, $\vec{\mathbf{U}}_1 = \frac{\rho_1}{\rho}\mathbf{U}$, $0 \leqslant \theta_1, \theta_2 \leqslant 1$ (in this paper, we set $\theta_1 = \theta_2 = 1$, so the scheme is fully explicit):

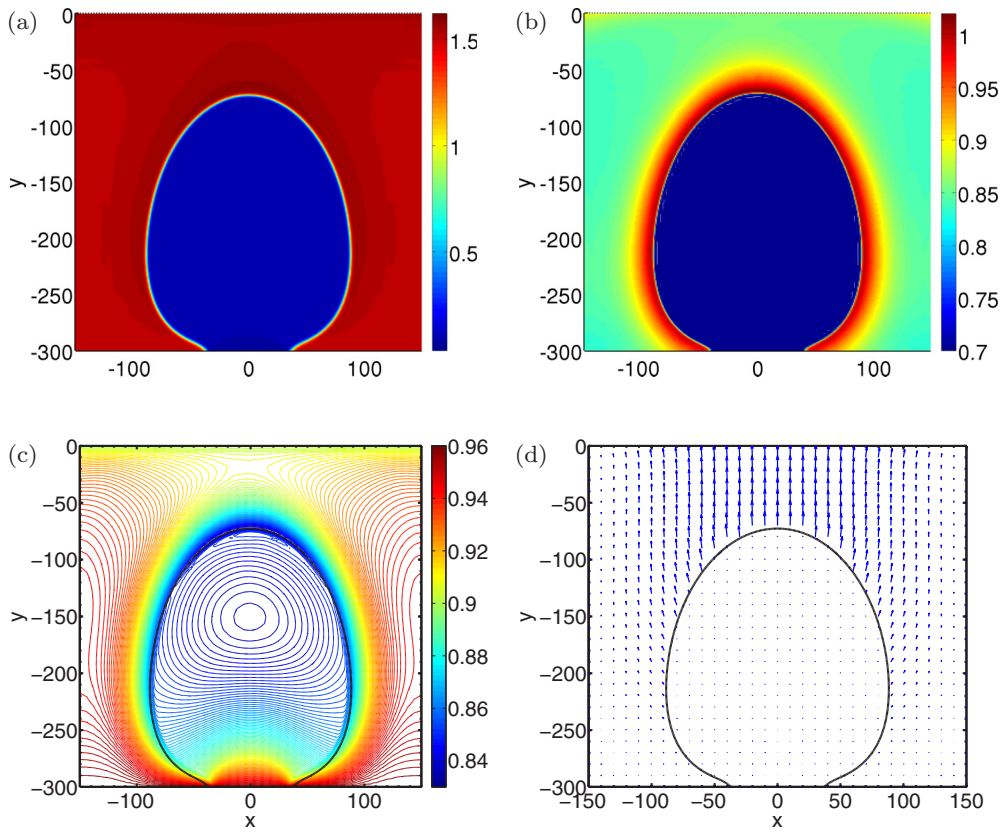

FIG. 8. (Color online) Case B: CO_2 + ethanol, open system, lyophilic surface; $t = 1500$. (a) Total density ρ, (b) density of ethanol ρ_1 (a minimum value 0.7 is set in order to show the variation of ρ_1 around the interface), (c) contour of temperature T; black line represents the interface, (d) total mass flux $\rho\vec{\mathbf{v}}$.

(1) Solve equation (51) to obtain the intermediate mass flux $\vec{\mathbf{U}}^*$,

$$\frac{\vec{\mathbf{U}}^* - \vec{\mathbf{U}}^n}{\triangle t} = \left[-\nabla\cdot(\vec{\mathbf{U}}\vec{\mathbf{v}}) + R\nabla\cdot\overleftrightarrow{P} + \frac{1}{\mathcal{R}e}\nabla\cdot\overleftrightarrow{\tau}\right]^n + \frac{\triangle t}{2}\vec{\mathbf{v}}^n\cdot\nabla[\nabla\cdot(\vec{\mathbf{U}}\vec{\mathbf{v}}) - R\nabla\cdot\overleftrightarrow{P}]^n. \quad (51)$$

(2) Solve equation (52) to obtain pressure tensor $\overleftrightarrow{P}^{n+1}$,

$$\overleftrightarrow{P}^{n+1} = \left[-p(\rho_1,\rho_2,T)\overleftrightarrow{\mathcal{I}} + \mathcal{L}_D\overleftrightarrow{\mathcal{I}} - \frac{\partial\mathcal{L}_D}{\partial\nabla\rho_1}\otimes\nabla\rho_1 - \frac{\partial\mathcal{L}_D}{\partial\nabla\rho_2}\otimes\nabla\rho_2\right]^n. \quad (52)$$

(3) Solve equation (53) to obtain difference between the generalized chemical potential $\hat{\mu}_1 - \hat{\mu}_2$,

$$(\hat{\mu}_1 - \hat{\mu}_2)^n = (\mu_1 - \mu_2)^n - \left(\sum_j \frac{T D_{1,j}}{m_1 m_j}\nabla^2\rho_j - \sum_j \frac{T D_{2,j}}{m_2 m_j}\nabla^2\rho_j\right)^n. \quad (53)$$

(4) Solve equation (54) to obtain density at the new time step ρ^{n+1},

$$\frac{\rho^{n+1} - \rho^n}{\triangle t} = -\nabla\cdot[\vec{\mathbf{U}}^n + \theta_1(\vec{\mathbf{U}}^* - \vec{\mathbf{U}}^n) + \theta_1\theta_2 R\triangle t\nabla\cdot(\overleftrightarrow{P}^{n+1} - \overleftrightarrow{P}^n)]. \quad (54)$$

(5) Solve equation (55) to obtain density of component 1 at the new time step ρ_1^{n+1},

$$\frac{\rho_1^{n+1} - \rho_1^n}{\triangle t} = -\nabla\cdot\left[\vec{\mathbf{U}}_1^n + \theta_1(\vec{\mathbf{U}}_1^* - \vec{\mathbf{U}}_1^n)\right] + \nabla\cdot\left[M_f\frac{\rho_1\rho_2}{\rho^2}\nabla\left(\frac{\hat{\mu}_1 - \hat{\mu}_2}{T}\right)\right]^n. \quad (55)$$

(6) Solve equation (56) to obtain mass flux at the new time step $\vec{\mathbf{U}}^{n+1}$,

$$\frac{\vec{\mathbf{U}}^{n+1} - \vec{\mathbf{U}}^*}{\triangle t} = R\nabla\cdot[\theta_2(\overleftrightarrow{P}^{n+1} - \overleftrightarrow{P}^n)] - \frac{\triangle t}{2}\vec{\mathbf{v}}^n\cdot\nabla\{R\nabla\cdot[\theta_2(\overleftrightarrow{P}^{n+1} - \overleftrightarrow{P}^n)]\}. \quad (56)$$

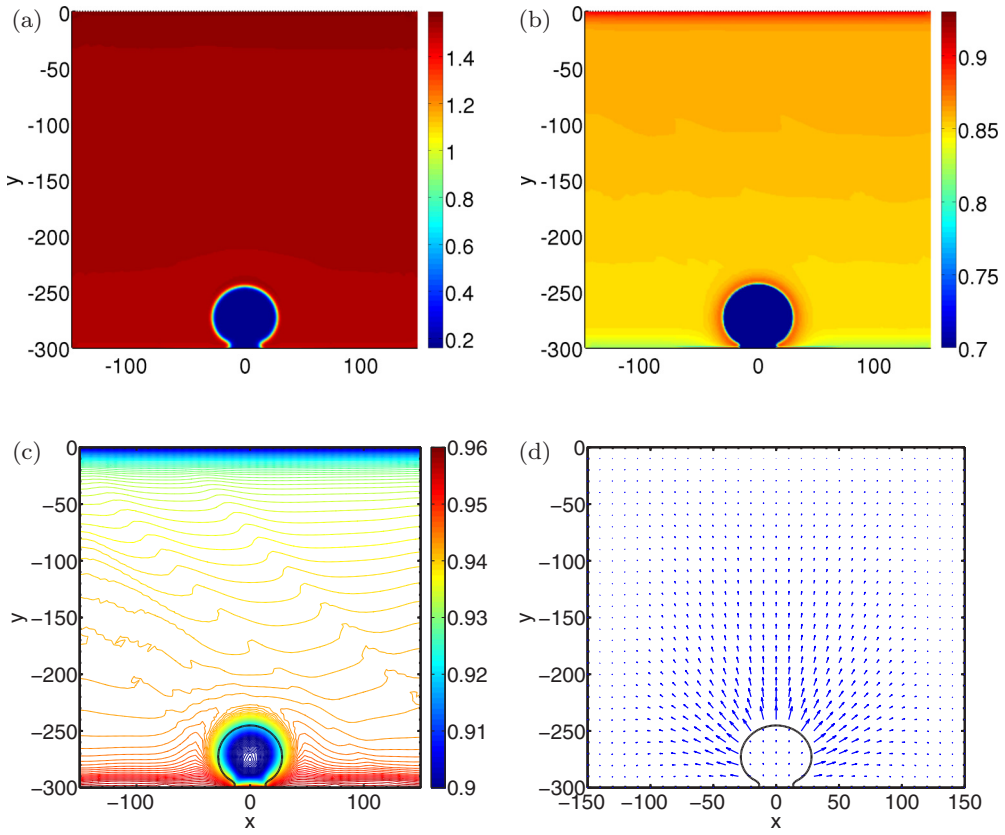

FIG. 9. (Color online) Case C: CO_2 + ethanol, closed system, lyophobic surface, $t = 100$. (a) Total density ρ, (b) density of ethanol ρ_1 (a minimum value 0.7 is set in order to show the variation of ρ_1 around the interface), (c) contour of temperature T; black line represents the interface, (d) total mass flux $\rho\vec{\mathbf{v}}$.

(7) Solve equation (57) to obtain the temperature at the new time step,

$$\begin{aligned}&\frac{(\rho e_T)^{n+1} - (\rho e_T)^n}{\triangle t}\\ &= \Big\{-\nabla\cdot(\rho e_T\vec{\mathbf{v}}) + \nabla\cdot[(\overleftrightarrow{P} + \mathcal{R}e^{-1}R^{-1}\overleftrightarrow{\tau})\cdot\vec{\mathbf{v}}]\\ &\quad + B\nabla\cdot[(\kappa_{12}\rho_1 + \rho_2)\nabla T]\\ &\quad - \sum_{i,j\in\{1,2\}}\nabla\cdot\left(\frac{T D_{i,j}}{m_i m_j}\frac{d\rho_i}{dt}\nabla\rho_j\right)\Big\}^n. \qquad (57)\end{aligned}$$

E. Verification of the wetting boundary condition

To verify the wetting boundary conditions (38) and (39) for the two-component system, we measure the apparent contact angle θ with time t for a simple isothermal system. Suppose a rectangular isothermal system is filled with a mixture of CO_2 and ethanol at $T = 0.957$, $P = 0.4$. Initially, the liquid and gas mixture is on the right and left half separately, with a straight interface in the middle, i.e., the initial contact angle is 90 degrees, as Fig. 2(a) shows. Assuming that the lower and the upper wall has an equilibrium angle $\theta_e = 45^\circ$ and $\theta_e = 135^\circ$ respectively, the interface at equilibrium would be a straight line. Figure 2(b) shows the interface profile at equilibrium. Figure 2(c) shows the way we extract the apparent contact angle. The solid line with red star represents the isocontour for the density $(\rho_g + \rho_l)/2$. The apparent contact angle is the angle between the isocontour and the solid wall, measured at a distance h above the solid wall, where h is the interfacial thickness. Figure 2(d) shows the difference between the measured contact angle θ and the equilibrium contact angle θ_e with time. It shows that the contact angle decreases very quickly initially due to the diffusion near the interface. It then decreases further, but at a much slower speed. Finally, at equilibrium, the difference between the contact angle and the equilibrium angle becomes very small.

To have a good balance between the computational cost and the accuracy of the solution, for all simulations in this paper, we use an adaptive mesh. Initially, the mesh is uniform and relatively coarse over the whole domain. It is then refined in the liquid-gas interfacial region during the evolution according to the local density gradient. Our previous paper about the rapid expansion process of CO_2 on a uniform mesh [36] has shown that the simulations were independent of the grid. For the adaptive mesh used in this paper, we check the influence of the initial uniform mesh size on the surface tension of CO_2 at $T = 0.9$ through Laplace tests. The initial mesh size Δx is set to 24, 12, and 6, respectively. The minimum mesh size h_m in the adaptive region is set to 1 for all cases. As shown in Fig. 3, surface tension σ does not change as Δx decreases from 12 to 6.

When using the Cahn–Hilliard model to simulate the interfacial problem for incompressible fluids, the model parameters α, β in the free-energy functional can be determined if the

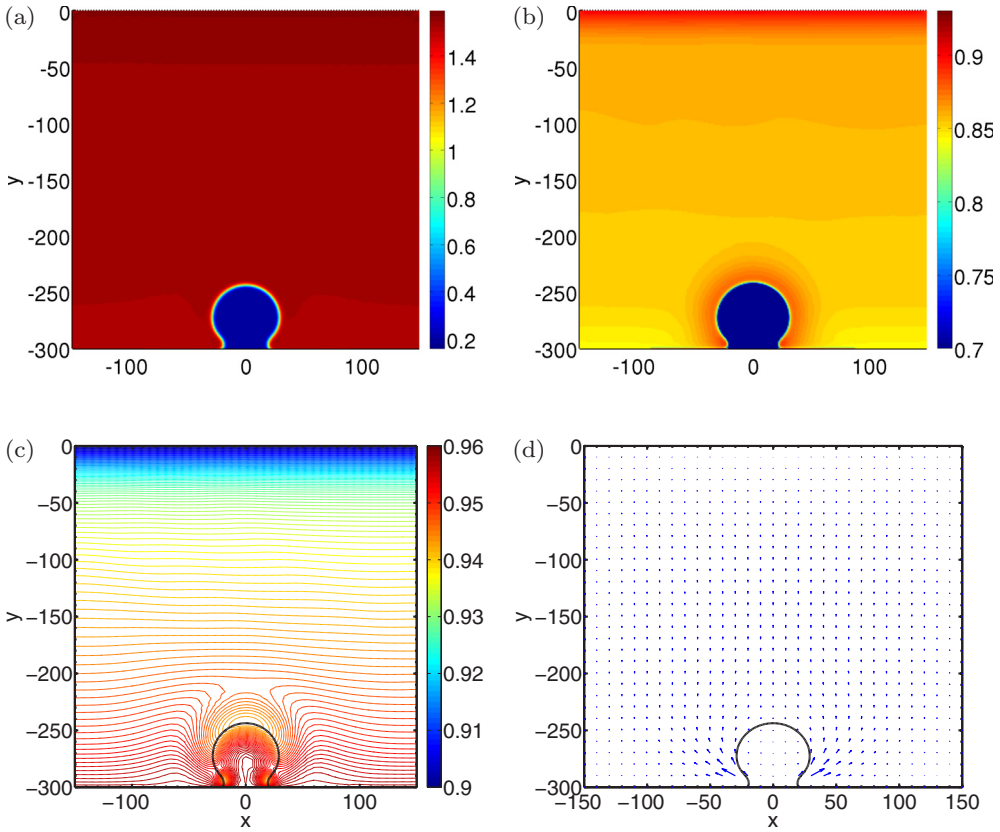

FIG. 10. (Color online) Case C: CO_2 + ethanol, closed system, lyophobic surface; $t = 300$. (a) Total density ρ, (b) density of ethanol ρ_1 (a minimum value 0.7 is set in order to show the variation of ρ_1 around the interface), (c) contour of temperature T; black line represents the interface, (d) total mass flux $\rho\vec{\mathbf{v}}$.

surface tension and the interfacial thickness are given, and vice versa. So the interfacial thickness can be arbitrarily chosen and enlarged. But for this new diffuse interface method for compressible fluid, there is no such simple relationship between those parameters. It is difficult to artificially enlarge the interfacial region. This sets a limitation in our simulation, i.e., the interfacial thickness in our simulation is, strictly speaking, the physical one, on the nanoscale. The capillary coefficient D_{ij} is related to both the surface tension and the interfacial thickness. We have shown in Ref. [27] that the numerical surface tension matches well with the experimental one for CO_2 + ethanol systems when we take $D_{11} = 12$ for ethanol, $D_{22} = 4$ for CO_2, and $D_{12} = 6.9282$. These values are also used in this paper, and the interfacial thickness is then determined automatically by these values of D_{ij}. Numerical results for the planar case show that, with $h_m = 1$, there are almost six grid points covering the interfacial region.

III. DYNAMICS OF BOILING

In this section, we show numerical results for the boiling process of a two-component fluid in a closed system and an open system, both for lyophilic and lyophobic surfaces. By "lyophilic" or "lyophobic," we mean that the contact angle formed between the interface and the solid wall on the liquid side is less or larger than 90°. In the following, the equilibrium contact angle θ_e is set to be 45° for a lyophilic surface, and 135° for a lyophobic surface. Notice that the wetting boundary conditions (38) and (39) derived in Sec. II C are for an isothermal system. For simplicity, we apply them here to simulate the boiling process which happens in nonisothermal systems, just as has been done for a one-component van der Waals fluid [12].

When the bottom wall is heated, the temperature there and the density of each component might change. This might cause the surface tension between the liquid and gas mixture to change too, resulting in the boundary conditions (38) and (39) being not as accurate as in an isothermal system. However, our numerical results in this section shows that, even in a heated system, the boundary conditions (38) and (39) can still be used as a good approximation.

The computational domain is two dimensional, $\Omega = [-150,150] \times [-300,0]$. Since $L^* = 8.287e - 10m$, our system is very small, thus the gravity effect can be ignored. Carbon dioxide is considered as component 2, and ethanol is considered as component 1. Initially, the temperature is linearly distributed from $T = 0.957$ at the bottom wall to $T = 0.9$ at the top wall. The density of each component over the whole domain is the saturated density of the binary system at $T = 0.957$, $P = 0.4$, which is $\rho_1^g = 0.0276$, $\rho_2^g = 0.1712$ for the gas mixture in the bubble, and $\rho_1^l = 0.8512$, $\rho_2^l = 0.6734$ for the liquid-mixture surroundings the bubble. The total density is thus $\rho^g = 0.1988$ in the bubble and $\rho^l = 1.5246$ in the liquid. With those conditions, the dimensionless parameters in the model are $\mathcal{R}e = 1.2506$, $\mathcal{R} = 0.5617$, $\mathcal{B} = 18.8598$, $\eta_{12} = 27.4550$, $\lambda_{12} = 0.2244$, $m_{21} = 0.8356$,

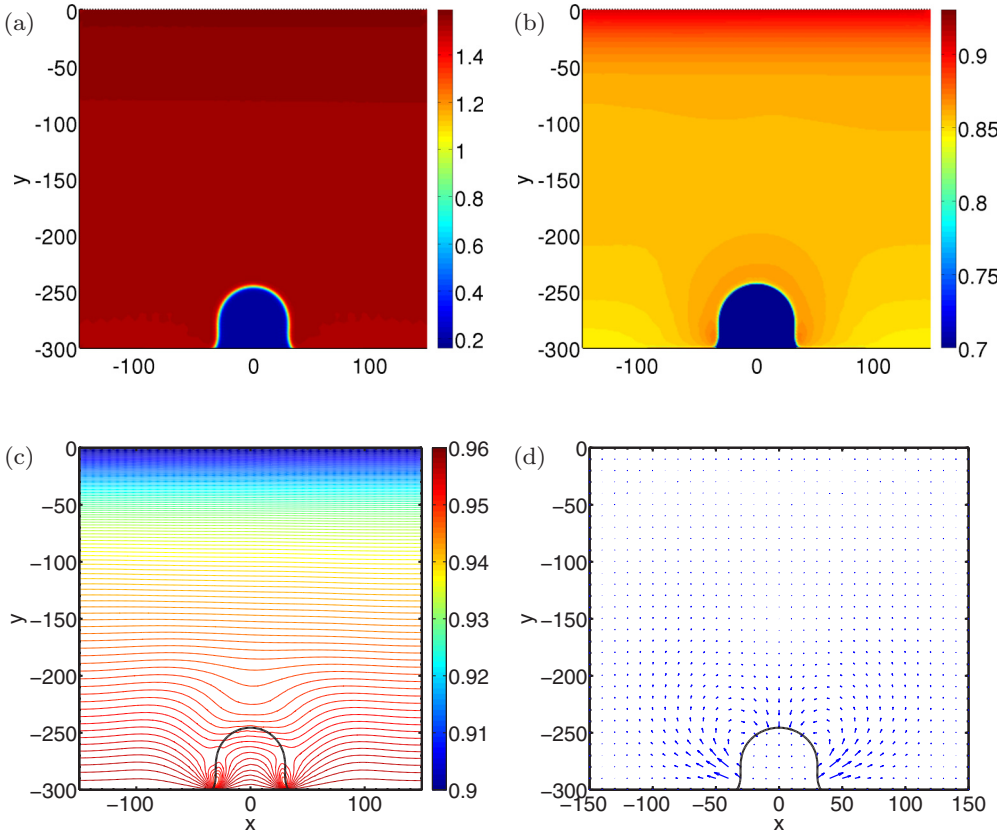

FIG. 11. (Color online) Case C: CO_2 + ethanol, closed system, lyophobic surface; $t = 1000$. (a) Total density ρ, (b) density of ethanol ρ_1 (a minimum value 0.7 is set in order to show the variation of ρ_1 around the interface), (c) contour of temperature T; black line represents the interface, (d) total mass flux $\rho\vec{\mathbf{v}}$.

$b_1 = 2.0276$, $a_{11} = 3.4262$, $a_{12} = 1.75$, $D_{11} = 12$, $D_{22} = 4$, $D_{12} = 6.9282$, $\sigma = 1.7992$. Figure 4 shows the initial profile of the density ρ of the mixture [Fig. 4(a)], the density ρ_1 of the component 1 [Fig. 4(b)], and the temperature T of the system [Fig. 4(c)] for all of our simulations in this section.

In all simulations, the temperature at the top and bottom boundaries are kept constant. The left and right boundaries are insulated walls with no heat flux. No slip condition for the velocity is imposed on all walls. In the open system, we allow mass flux to flow out of the top boundary.

A. Open system, lyophobic surfaces

First, let us consider the evolution of a mixture-gas bubble on a lyophobic surface in the open system. By "open system" we mean that the top boundary is open, and the fluid can flow out of the system through the open boundary. The bottom wall attracts the gas phase more strongly than the liquid phase. Figures 5 and 6 show the total density ρ of the mixture, the density ρ_1 of component 1, the temperature T, and the mass flux $\rho\vec{\mathbf{v}}$ at different stages. For each variable, we use the same color bar in order to have a good comparison. To show the variation in the density of component 1, we set a threshold 0.7 as the minimum value when we plot ρ_1. The real value of ρ_1 in the gas bubble is usually less than 0.1.

Figure 5(a) shows that, as the bubble spreads on the bottom wall, it also quickly grows. Figure 5(b) shows that, around the interface, there is a thin layer where the density of ethanol in the liquid phase increases. The preferential evaporation of the more volatile component is a typical phenomenon in the binary boiling problems [37]. Around the interface, the phase changes from liquid to gas for both CO_2 and ethanol. Since CO_2 is more volatile, more liquid CO_2 changes to gas CO_2 or, in other words, more liquid ethanol remains in the liquid mixture, resulting in an increased density of ethanol in the liquid from 0.1712 at $t = 0$ to greater than 0.9 at $t = 500$. Figure 5(c) shows that, as the bubble grows, the temperature within the bubble decreases a lot due to the latent heat absorbed, except for the region just above the bottom wall. Corresponding to the thin layer around the bubble where the density of ethanol increases, the temperature there is higher than in the gas bubble, but lower than other parts of the liquid. Due to the fact that the heat conductivity of the gas is much smaller than that of the liquid, the temperature variation in the gas is much larger than in the liquid. Figure 5(d) shows the mass flux in the open system. The mass flux in the gas phase is very small. But there is a large mass flux in the interfacial region and the liquid region. Phase change happens mainly in the interfacial region, so we can see large mass flux there. As the bubble grows, it pushes the liquid out of the system through the top boundary, which then results in the mass flux in the liquid mixture.

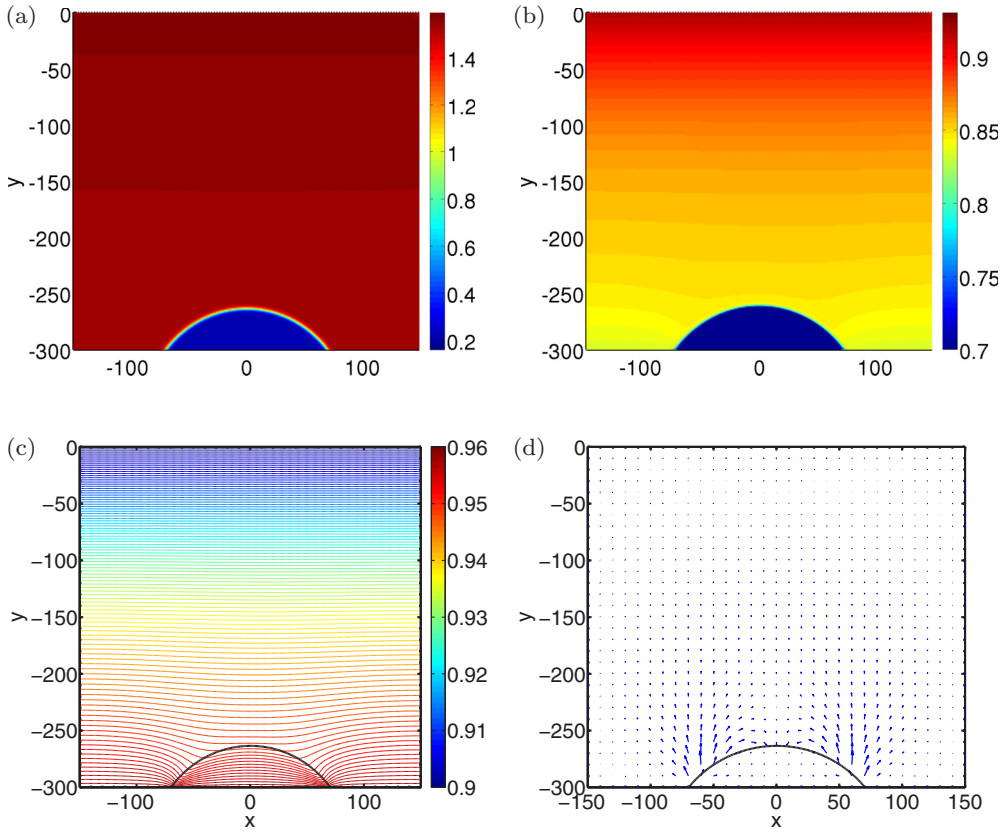

FIG. 12. (Color online) Case C: CO_2 + ethanol, closed system, lyophobic surface; $t = 8000$. (a) Total density ρ, (b) density of ethanol ρ_1 (a minimum value 0.7 is set in order to show the variation of ρ_1 around the interface), (c) contour of temperature T; black line represents the interface, (d) total mass flux $\rho\vec{\mathbf{v}}$.

Figure 6 shows the total density ρ, the density of ethanol ρ_1, the temperature T and total mass flux $\rho\vec{\mathbf{v}}$ at a much later time, $t = 1500$. It is seen that the bubble grows more rapidly than it spreads on the bottom wall. The denser ethanol in the thin liquid layer around the bubble is more obvious; see Fig. 6(b). The mass flux just above the top of the bubble is much larger than the mass flux in the foot region; see Fig. 6(d).

B. Open system, lyophilic surfaces

Next, we simulate binary boiling on a lyophilic surface for a open system. The bottom wall favors the liquid phase over the gas phase. The bubble, instead of spreading rapidly on the bottom wall, prefers to be rolled up; see Fig. 7 at $t = 500$. Except for the movement of the contact line, no other physical phenomena that are essentially different from the boiling on a lyophobic surface above are visible. For example, there is a thin layer around the bubble where the density of the ethanol becomes greater [Fig. 7(b)]. The temperature of the liquid in this thin layer is higher than the gas bubble, but lower than its surroundings liquid [Fig. 7(c)]. Also, the mass flux within the gas bubble is very small. Around the interface, there is a large mass flux pointing from the gas bubble to the liquid. From the foot region of the bubble to the top of the bubble, the mass flux increases. The liquid mixture in the domain is pushed out of the system due to the growth of the bubble [Fig. 7(d)].

Figure 8 shows the distribution of the total density ρ, the density of ethanol ρ_1, the temperature T, and the total mass flux $\rho\vec{\mathbf{v}}$ at a later time, $t = 1500$. Compared with Fig. 6, only the spreading distance of the moving contact line and the shape of the interface near the bottom wall are different; other physical characteristics are the same.

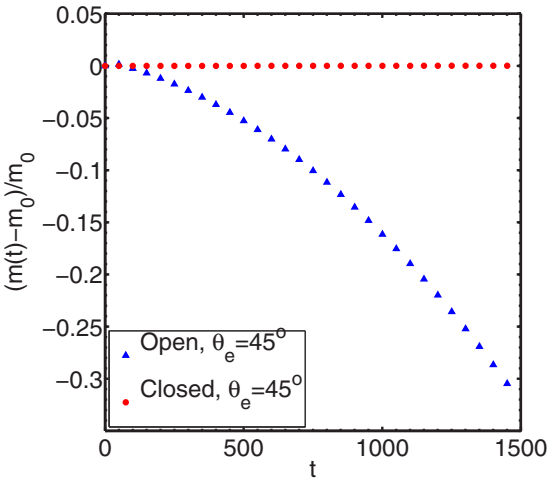

FIG. 13. (Color online) Relative change of the total mass $\frac{m(t)-m_0}{m_0}$ with time t. $m(t)$ is the total mass of the systems at time t, m_0 is the initial total mass.

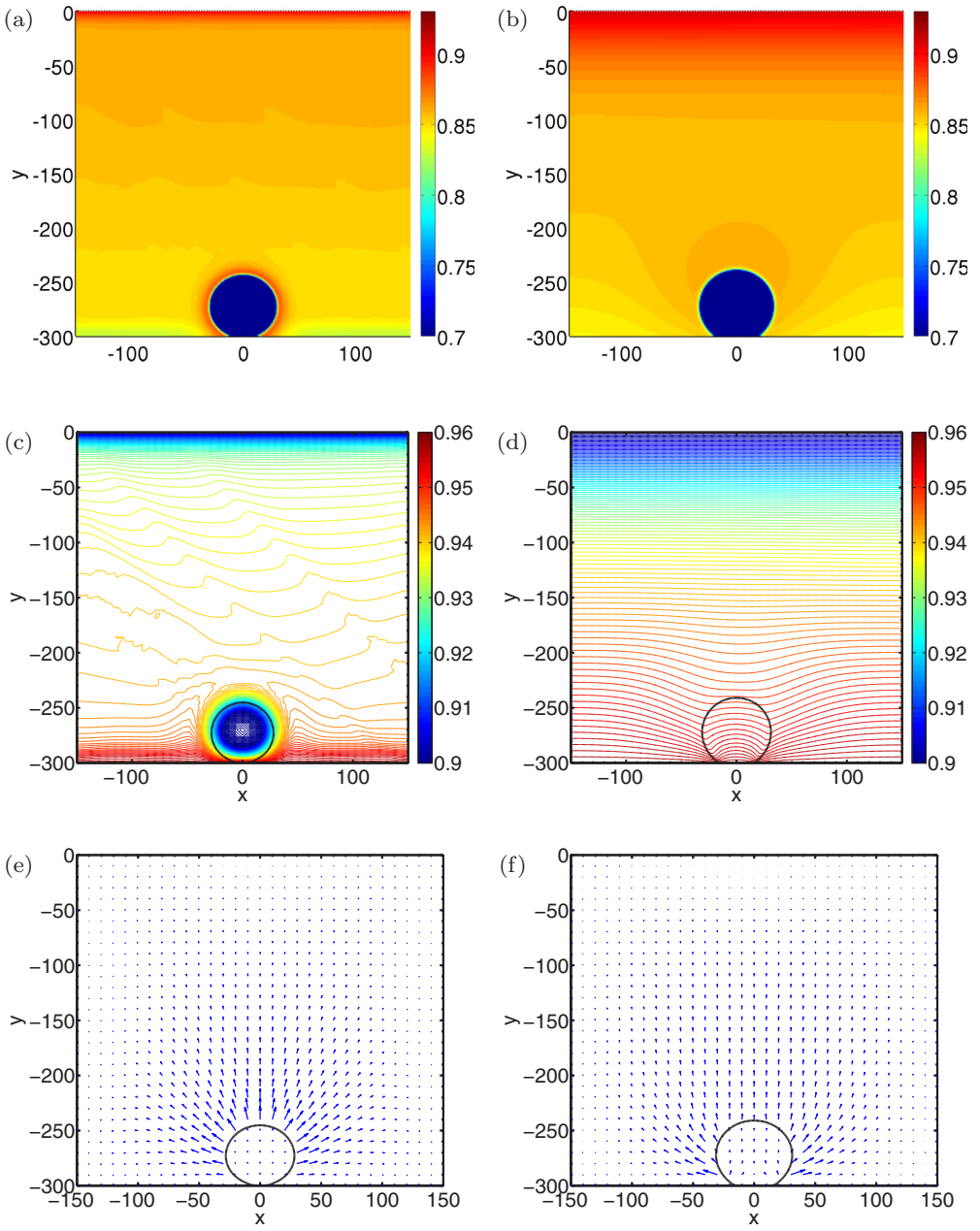

FIG. 14. (Color online) Case D: CO_2 + ethanol, closed system, lyophilic surface. (a) Density of ethanol ρ_1 at $t = 100$, (b) density of ethanol ρ_1 at $t = 2000$, (c) contour of temperature T at $t = 100$, (c) contour of temperature T at $t = 2000$, (e) total mass flux $\rho\vec{\mathbf{v}}$ at $t = 100$, (f) total mass flux $\rho\vec{\mathbf{v}}$ at $t = 2000$. For ρ_1 in panels (a) and (b), a minimum value 0.7 is set in order to show the variation around the interface.

C. Closed system, lyophobic surfaces

Binary boiling in a closed system shows very different dynamics. Unlike in the open system, where the thin layer with denser ethanol around the bubble exists and becomes more obvious during the whole evolution time, the thin layer in the closed system becomes thicker and less concentrated in ethanol very quickly and finally becomes indistinguishable from its surroundings. Figures 9–12 show the distribution of the total density ρ, the density of ethanol ρ_1, the temperature T, and the total mass flux $\rho\vec{\mathbf{v}}$ at different time. Figure 9(b) shows that at very early time $t = 100$, we can observe a very thin layer around the bubble as well as near the top wall where ethanol becomes denser. In a short time, ethanol in the denser region diffuses very quickly to its surroundings; see Figs. 10(b) and 11(b). At $t = 7000$, the thin layer around the bubble has disappeared, and the density of ethanol from the top wall to the bottom decreases smoothly, as Figure 12(b) shows. In the open system, temperature variation is obvious during the whole process, as the results in Secs. III A and III B show. But in the closed system, temperature variation is only appreciable in the early stage. Figure 9(c) tells us that, at $t = 100$, the temperature inside the bubble is lower, especially in the central region of the bubble. After a short while, at $t = 300$ [see Fig. 10(c)], the temperature in the central region of the bubble increases to the same temperature as on the

bottom wall, except for a relative low temperature in the layer around the bubble as well as near the foot region. As the boiling process proceeds, the thin layer around the bubble disappears, and the temperature in the foot region of the bubble becomes almost the same as its surroundings; see Figs. 11(c) and 12(c). For the mass flux in the open system, we have not observed any vortices during the whole boiling process, so it is a pure evaporation process. In the closed system, we can clearly see from Fig. 11(d) that two vortices have already been generated around the bubble at $t = 1000$, indicating evaporation near the foot region of the bubble and condensation at the top of the bubble. As the bubble spreads, these two vortices persist and move, as Fig. 12(d) shows.

A big difference between the open and the closed system is that the pressure increases in the closed system. For the boiling of a pure fluid, this would increase the boiling temperature and thus delay the nucleation process. In this paper, we do not consider the early nucleation process. Instead, we start from the point where a bubble has already formed in the system. For the boiling of a binary fluid, the increase of pressure would change the equilibrium composition of each component in the liquid and gas phase. We have shown [27] that for the binary system CO_2 + ethanol, as pressure increases, the mass fraction of CO_2 in the liquid phase would increase. This might be the reason why the preferential evaporation of CO_2 in the open system is much more obvious than in the closed system, as Figs. 6(b) and 11(b) show.

Another difference between the open and the closed system is the change of the total mass of the system. Figure 13 gives the relative change of the total mass $\frac{m(t)-m_0}{m_0}$ with time t. Red circles represent the closed system, blue upward triangles represent the open system. The total mass decreases in the open system since the growing bubble takes more and more space. In the closed system, no fluid can escape, so the total mass does not change.

D. Closed system, lyophilic surfaces

By making the bottom wall attract the liquid mixture more than the gas mixture, the gas bubble would not spread much. Basic characteristics like a thin layer with denser ethanol around the bubble and the variation of temperature are also visible at early times, such as $t = 100$; see Figs. 14(a) and 14(c). Those characteristics disappear at later times, such as $t = 2000$, see Figs. 14(b) and 14(d), just the same as the boiling on the lyophobic surface in Sec. III C. However, the phenomenon we have observed on a lyophobic surface in Fig. 10(c) that the temperature is relative low near the foot region of the bubble at early time has not been observed on a lyophilic surface. Furthermore, the mass flux does not show any vortices during the whole process; see Figs. 14(e) and 14(f).

We measure the apparent contact angle and compare it with the equilibrium contact angle we set. Figure 15 shows that, as time passes, the difference between the apparent contact angle and the equilibrium angle approaches zero.

IV. DISCUSSION

There are several possible mechanisms through which heat is transferred and the bubble grows, such as the evaporation of a thin microlayer of liquid which might form between a growing, hemispherically shaped bubble and the superheated wall, or the evaporation of the superheated liquid layer surrounding the bubble cap, or the evaporation of the liquid at the contact line, or microconvection [38]. Although all of those mechanisms contribute to the bubble heat transfer to some degree, there is not a single model available which can incorporate all these submodels [38]. For the numerical simulation of bubble growth in the literature, some were based on an assumed heat transfer mechanism, like the work done by Lee and Nydahl [39], some treated the microregion and the macroregion separately, like the work done by Son *et al.* [40], or Kern and Stephan [37]. In this paper, no assumption on the heat transfer mechanism is made and the whole computational domain is treated the same. All phenomena appear naturally as a result of the model and the simulation. In this paper, we are not concerned with details of the heat-transfer mechanisms, but we want to point out that, in all the cases considered in this paper, we have not observed a microlayer below the bubble. Previous studies on boiling using diffuse interface method have not reported such a microlayer, either [3,12]. This might due to the diffuse interface model itself, or due to the parameters used in the model.

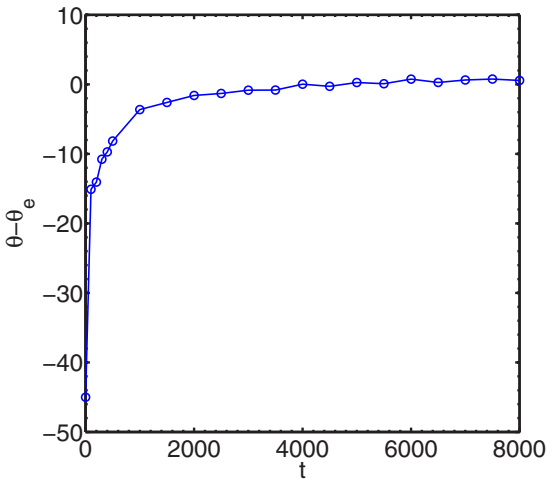

FIG. 15. (Color online) $\theta - \theta_e$ vs time t for CO_2 + ethanol mixture in the closed system on a lyophilic surface.

V. CONCLUSION

We have presented numerical results of boiling of CO_2 + ethanol mixture in open and closed systems, on both lyophilic and lyophobic surfaces, based on a two-component diffuse interface model. Wetting boundary conditions for an isothermal, two-component system are also derived and verified, following the same methodology used in the Cahn–Hilliard modeling of wetting [29] and the boiling of a pure van der Waals fluid [12]. For a nonisothermal system, a more sophisticated and accurate wetting boundary condition might be needed to take into account the variation of density, temperature, and surface tension near the bottom wall. But our numerical results show that the derived boundary conditions could also serve as a good approximation even in a boiling system, where the temperature is nonuniform.

Our model is able to capture the typical phenomena in binary boiling, i.e., the preferential evaporation of the more volatile component. For the CO_2 + ethanol mixture, we observed that there is a thin layer around the bubble where the density of ethanol increases. The temperature within this layer is higher than that of the bubble but lower than its surroundings. The evolution of those physical characteristics in an open systems is very different from a closed system. The thin layer becomes more obvious in the open system as time progresses and exists during the whole process. In the closed system, however, this layer becomes less concentrated in early time and finally disappears. Similarly, temperature variation in the open system is obvious during the whole process. But in the closed system, the temperature variation is only appreciable in the early stage, and the temperature quickly becomes nearly uniform close to the bottom wall. Moreover, vortices are never generated in the open system, but we observed vortices in the closed system on a lyophilic surface.

For boiling in an open system, except for the difference in the movement of the contact line, other essential physical characteristics, such as the evolution of the composition, the temperature, or the mass flux, do not differ strongly between lyophilic surfaces and lyophobic surfaces. In the closed system, however, the vortices that are observed on a lyophobic surface are not observed on a lyophilic surface.

ACKNOWLEDGMENT

The authors acknowledge computer time provided by SNIC (Swedish National Infrastructure for Computing) and the support from the PRACE-3IP project (FP7 RI-312763).

[1] L. H. Chai, X. F. Peng, and D. Lee, Interfacial effects on nucleate boiling heat transfer of binary mixtures, Int. J. Therm. Sci. **40**, 125 (2001).

[2] Y. Fujita and Q. Bai, Critical heat flux of binary mixtures in pool boiling and its correlation in terms of Marangoni number, Int. J. Refrig. **20**, 616 (1997).

[3] X. Xu and T. Qian, Single-bubble dynamics in pool boiling of one-component fluids, Phys. Rev. E **89**, 063002 (2014).

[4] G. Tomar, G. Biswas, A. Sharma, and A. Agrawal, Numerical simulation of bubble growth in film boiling using a coupled level-set and volume-of-fluid method, Phys. Fluids **17**, 112103 (2005).

[5] H. Inaoka and N. Ito, Numerical simulation of pool boiling of a Lennard-Jones liquid, Phys. A (Amsterdam, Neth.) **392**, 3863 (2013).

[6] T. Seta and K. Okui, The single component thermal lattice Boltzmann simulation of pool boiling in two dimensions, J. Therm. Sci. Technol. (Tokyo, Jpn.) **1**, 125 (2006).

[7] Y. Tanaka, M. Yoshino, and T. Hirata, Lattice Boltzmann simulation of nucleate pool boiling in saturated liquid, Commun. Comput. Phys. **9**, 1347 (2011).

[8] G. Son and V. K. Dhir, Numerical simulation of film boiling near critical pressures with a level set method, J. Heat Transfer **120**, 183 (1998).

[9] A. Mukherjee and S. G. Kandlikar, Numerical study of single bubbles with dynamic contact angle during nucleate pool boiling, Int. J. Heat Mass Transfer **50**, 127 (2007).

[10] C. Kunkelmann and P. Stephan, CFD simulation of boiling flows using the volume-of-fluid method within OpenFOAM, Numer. Heat Transfer, Part A **56**, 631 (2009).

[11] C. Kunkelmann and P. Stephan, Numerical simulation of the transient heat transfer during nucleate boiling of refrigerant HFE-7100, Int. J. Refrig **33**, 1221 (2010).

[12] T. Laurila, A. Carlson, T. Ala-Nissila, M. Do-Quang, and G. Amberg, Thermohydrodynamics of boiling in a van der Waals fluid, Phys. Rev. E **85**, 026320 (2012).

[13] G. Tryggvason, B. Bunner, A. Esmaeeli, D. Juric, N. Al-Rawahi, W. Tauber, J. Han, S. Nas, and Y.-J. Jan, A front-tracking method for the computations of multiphase flow, J. Comput. Phys. **169**, 708 (2001).

[14] C. Hirt and B. Nichols, Volume of fluid (VOF) method for the dynamics of free boundaries, J. Comput. Phys. **39**, 201 (1981).

[15] R. Scardovelli and S. Zaleski, Direct numerical simulation of free-surface and interfacial flow, Annu. Rev. Fluid Mech. **31**, 567 (1999).

[16] S. Osher and R. P. Fedkiw, Level set methods: An overview and some recent results, J. Comput. Phys. **169**, 463 (2001).

[17] J. A. Sethian and P. Smereka, Level set methods for fluid interfaces, Annu. Rev. Fluid Mech. **35**, 341 (2003).

[18] D. M. Anderson, G. B. McFadden, and A. A. Wheeler, Diffuse-interface methods in fluid mechanics, Annu. Rev. Fluid Mech. **30**, 139 (1998).

[19] H. Ding, P. D. M. Spelt, and C. Shu, Diffuse interface model for incompressible two-phase flows with large density ratios, J. Comput. Phys. **226**, 2078 (2007).

[20] C. Liu, J. Shen, and X. Yang, Decoupled energy stable schemes for a phase-field model of two-phase incompressible flows with variable density, J. Sci. Comput. **62**, 601 (2015).

[21] P. Yue, J. J. Feng, C. Liu, and J. Shen, A diffuse-interface method for simulating two-phase flows of complex fluids, J. Fluid Mech. **515**, 293 (2004).

[22] J. Shen, X. Yang, and Q. Wang, Mass-conserved phase field models for binary fluids, Commun. Comput. Phys. **13**, 1045 (2013).

[23] J. D. Van der Waals, Verh.-K. Ned. Akad.Wet., Afd. Natuurkd., Eerste Reeks **1**, 56 (1893).

[24] J. W. Cahn and J. E. Hilliard, Free energy of a nonuniform system. III. Nucleation in a two-component incompressible fluid, J. Chem. Phys. **31**, 688 (1959).

[25] A. Onuki, Dynamic van der Waals theory, Phys. Rev. E **75**, 036304 (2007).

[26] A. Onuki, Henry's law, surface tension, and surface adsorption in dilute binary mixtures, J. Chem. Phys. **130** 124703 (2009).

[27] J. Liu, G. Amberg, and M. Do-Quang Diffuse interface method for a compressible binary fluid (unpublished).

[28] D. Wheeler, J. A. Warren, and W. J. Boettinger, Modeling the early stages of reactive wetting, Phys. Rev. E **82**, 051601 (2010).

[29] D. Jacqmin, Calculation of two-phase Navier–Stokes flows using phase-field modeling, J. Comput. Phys. **155**, 96 (1999).

[30] C. I. Poser and I. C. Sanchez, Interfacial tension theory of low and high molecular weight liquid mixtures, Macromolecules (Washington, DC, US) **14**, 361 (1981).

[31] A. Carlson, Capillarity and dynamic wetting, Ph.D. thesis, Royal Institute of Technology, Sweden, 2012 (unpublished).

[32] B. S. Carey, L. E. Scriven, and H. T. Davis, Semiempirical theory of surface tension of binary systems, AIChE J. **26**, 705 (1980).

[33] G. Amberg, R. Tönhardt, and C. Winkler, Finite element simulations using symbolic computing, Math. Comp. Simul. **49**, 257 (1999).

[34] W. Bangerth, T. Heister, L. Heltai, G. Kanschat, M. Kronbichler, M. Maier, B. Turcksin, and T. D. Young, The deal.II library, version 8.2, Archive of Numerical Software, **3**(100), 1 (2015).

[35] J. Liu, G. Amberg, and M. Do-Quang, Numerical simulation of particle formation in the rapid expansion of supercritical solution process, J. Supercrit. Fluids **95**, 572 (2014).

[36] J. Liu, M. Do-Quang, and G. Amberg, Numerical simulation of rapid expansion of supercritical carbon dioxide, AIChE J. **61**, 317 (2015).

[37] J. Kern and P. Stephan, Theoretical model for nucleate boiling heat and mass transfer of binary mixtures, J. Heat Transfer **125**, 1106 (2003).

[38] J. Kim, Review of nucleate pool boiling bubble heat transfer mechanisms, Int. J. Multiphase Flow **35**, 1067 (2009).

[39] R. C. Lee and J. E. Nydahl, Numerical calculation of bubble growth in nucleate boiling from inception through departure, J. Heat Transfer **111**, 474 (1989).

[40] G. Son, V. K. Dhir, and N. Ramanujapu, Dynamics and heat transfer associated with a single bubble during nucleate boiling on a horizontal surface, J. Heat Transfer **121**, 623 (1999).